

Thermal Evolution of Structures and Conductivity of Pr-substituted $\text{BaZr}_{0.7}\text{Ce}_{0.2}\text{Y}_{0.1}\text{O}_{3-\delta}$: Potential Cathode Components for Protonic Ceramic Fuel Cells

Gemma Heras-Juaristi^a, Ulises Amador^b, Rodolfo O. Fuentes^c, Adilson L. Chinelatto^d, Julio Romero de Paz^e, Clemens Ritter^f, Duncan P. Fagg^g, Domingo Pérez-Coll^h, Glenn C. Mather^{a*}

^aInstituto de Cerámica y Vidrio, CSIC, Cantoblanco, 28049 Madrid, Spain

^bQuímica Facultad de Farmacia, Universidad CEU-San Pablo, Boadilla del Monte, Madrid 28668, Spain

^cDept. de Física de la Materia Condensada, CNEA, Av. Gral. Paz 1499, 1650 Buenos Aires, Argentina

^dDept. de Engenharia de Materiais, Universidade Estadual de Ponta Grossa, Av. Gal. Carlos Cavalcanti, 4748, 84030-900- Ponta Grossa-PR, Brazil

^eC.A.I. Técnicas Físicas, Facultad de Ciencias Físicas, Universidad Complutense, 28040 Madrid, Spain

^fInstitut Laue-Langevin, 71 Avenue des Martyrs, Grenoble 38042, France

^gDepartment of Mechanical Engineering, University of Aveiro, 3810-193 Aveiro, Portugal

Abstract

A complete solid solution forms between the perovskite proton conductor $\text{BaZr}_{0.7}\text{Ce}_{0.2}\text{Y}_{0.1}\text{O}_{3-\delta}$ (BZCY72) and $\text{BaPr}_{0.9}\text{Y}_{0.1}\text{O}_{3-\delta}$ (BPY) on synthesis by the citrate method and high-temperature annealing. Phase fields of selected members of the $\text{Ba}(\text{Ce}_{0.2}\text{Zr}_{0.7})_{1-x}\text{Pr}_x\text{Y}_{0.1}\text{O}_{3-\delta}$ series were studied as a function of composition and temperature by high-resolution neutron powder diffraction revealing symmetry changes in the sequence $Pnma \rightarrow Imma \rightarrow R\bar{3}c \rightarrow Pm\bar{3}m$. Higher symmetry is favoured for low Pr contents and high temperatures, as consideration of tolerance factor suggests. A volume contraction, ascribed to dehydration, is observed by synchrotron X-ray diffraction on heating in air for lower x. Magnetic measurements and structural data support the presence of Pr in the IV valence state on the perovskite B site. Thermogravimetric analysis in CO_2 to ~ 980 °C indicates better chemical stability for $x \leq 0.445$, whereas decomposition occurred for higher x. Electrical conductivity increases by over two orders of magnitude in dry air from $x = 0.225$ to 0.675 ($\sigma \sim 0.4 \text{ S}\cdot\text{cm}^{-1}$ at 900 °C for $x = 0.675$). Electron-hole transport with a positive $p\text{O}_2$ dependence, consistent with an “extrinsic” model of acceptor-dopant charge compensation by oxygen vacancies is found for the series; the activation energy for thermally activated hole hopping in air in the range 250 - 500 °C decreases from ~ 1 eV for BZCY72 to ~ 0.4 eV for $x = 0.675$. Conductivity is generally lower in humidified N_2 and air ($p\text{H}_2\text{O} \approx 0.023$ atm) than in the corresponding dry atmosphere, consistent with consumption of holes by less

mobile protonic species; however for $x \leq 0.225$ the lower electronic conductivity in N_2 results in slightly higher conductivity in wet conditions.

Introduction

Proton conduction at high temperatures in ceramic materials offers unique opportunities for membrane technologies involving the separation of hydrogen or its conversion to electrical energy in protonic ceramic fuel cells (PCFCs) ¹⁻³. Example applications of membranes based on proton-conducting ceramics include the reduction of CO_2 ⁴, separation of hydrogen from syn gas ⁵ or, as recently demonstrated, for the non-oxidative conversion of natural gas to aromatics through the process of methane dehydroaromatization ⁶.

PCFCs cleanly convert the chemical energy of hydrogen to electrical energy in an intermediate temperature range, which avoids the costs associated with the higher operating temperatures of oxide-ion conducting solid oxide fuel cells (SOFCs) and those of the polymer-based devices which require expensive noble-metal catalysts. Hydrogen remains undiluted in protonic ceramic cells in both fuel cell and electrolysis mode, with the advantages that no further recycling is required and Ni in the hydrogen electrode remains at a suitably low oxygen partial pressure to prevent its oxidation ^{7,8}.

For PCFCs and membrane reactors, barium cerium-zirconate solid solutions with the perovskite (ABO_3) structure have emerged as the strongest candidate electrolytes. Particular attention is paid to the composition $BaZr_{0.7}Ce_{0.2}Y_{0.1}O_{3-\delta}$ (BZCY72) which offers a useful compromise of moderately high proton conductivity and good stability associated with the $BaCe_{0.9}Y_{0.1}O_{3-\delta}$ and $BaZr_{0.9}Y_{0.1}O_{3-\delta}$ end-member phases, respectively ^{6,9,10}.

Lowering the operating temperature in PCFCs produces much larger overpotentials at the electrode/electrolyte interface. The cathode plays a most important role in establishing the fuel efficiency of fuel-cell operation at the intermediate temperature of operation of PCFCs since the reaction kinetics for oxygen migration are slower than the kinetics related to fuel oxidation in the anode

or ion migration in the electrolyte. Different strategies have been employed so far with respect to PCFC cathodes. These include adopting a mixed oxide ion-electron conductor as in a classical SOFC cathode¹¹⁻¹⁴, improving the electronic conductivity of a proton conductor through doping¹⁵, designing materials with potential for conduction of protons, electron and oxide-ions¹⁶, or a mixed approach involving a composite material with proton and oxide-ion-electron-conducting components^{17,18}. Although it is still unclear which route proves to be the most successful, materials which have both high proton and electron conductivity with the requisite stability for use as component parts of cathodes or other high-temperature electrochemical applications are important contemporary materials deserving detailed investigation.

Praseodymium is an interesting dopant for perovskite-based proton conductors since, depending on concentration levels, considerable electron-hole conductivity is generated, of interest for the air electrode of ceramic fuel cells^{19,20} and other mixed transport applications. In contrast, low levels of Pr doping, which increase the sinterability of barium zirconate-based proton conductor, do not significantly increase p-type transport²¹. Recent work has shown that the Pr IV valence state may be stabilized for a small average B-site cation radius, which could explain the low-dopant-level behaviour²². However, Pr-rich perovskite solid-solution members typically show poor stability in wet and reducing gases²³⁻²⁵, so choosing the best dopant level for a particular system is critical.

In this regard, mapping the structural phase transitions that may take place with temperature and composition in complex perovskite systems, such as those mentioned, is of interest for correlation with their technologically relevant properties and further development. Recently, we reported the phase transitions which occur in BZCY72, which displays a first-order transformation from orthorhombic (space group *Imma*) to rhombohedral symmetry ($R\bar{3}c$) between 85 and 150 K then a further transition to cubic symmetry (*Pm* $\bar{3}m$) at ~ 570 K²⁶. Here, as part of the present work, we extend this structural study to solid-solution members in the BZCY72-BaPrO₃ system with potential application as mixed protonic-electronic conductors, particularly as PCFC cathode components and

membrane reactors. High-resolution neutron powder diffraction (NPD) complemented by synchrotron radiation X-ray diffraction (SR-XRD) is employed to perform a detailed structural analysis in the temperature range RT–900°C for selected compositions, involving space-group determination and phase transitions with temperature. Structural studies are complemented by magnetic measurements to investigate the Pr oxidation state. Impedance-spectroscopy data for the series are collected in dry and humidified air and N₂ atmospheres, and the electrical-transport properties discussed in terms of the prevailing defect chemistry and structural information.

Experimental

Samples in the series Ba(Ce_{0.2}Zr_{0.7})_{1-(x/0.9)}Pr_xY_{0.1}O_{3-δ} (x = 0, 0.225, 0.445, 0.675, 0.9) were prepared by a citrate process based on the Pechini method. Prior to synthesis, the water content of the nitrate precursors was determined by thermogravimetry in air. The appropriate stoichiometric ratio of nitrates was added in the order Ba(NO₃)₂.xH₂O, ZrO(NO₃)₂.xH₂O, Ce(NO₃)₃.xH₂O, Y(NO₃)₃.xH₂O and Pr(NO₃)₃.xH₂O to deionised water heated at ~ 50 °C on a hotplate. Once a transparent green solution was obtained, the temperature was raised first in the range 60-80 °C for ~ 2 hours then again to > 90 °C for 4-5 hours, and finally to above 100 °C for over 12 hours. The resulting dark-brown polymerized complex was subsequently pyrolysed in an oven at 350 °C for 4 h. The obtained polymeric precursor was then heated at 600 °C for 4 h, milled and heat treated at 1100 °C for a further 4 h to remove any remaining organic product, prior to attrition milling in a teflon vial with zirconia balls and sieving (100 μm). Material for phase analysis and structural characterisation was then prepared in powder form or by firstly pressing the as-prepared powder into pellets, covering with sacrificial powder of the same composition and firing in the range 1350-1500 °C for 4 hours. The pellets were then crushed and milled in an agate mortar and pestle in acetone.

Ceramic bodies were observed to disintegrate after several days' exposure to laboratory air suggesting that some carbonation or hydration of Ba had occurred. Typically, the presence of only a

very small amount of unreacted basic oxide below that detected at the resolution of XRD is sufficient to bring about such mechanical fragility. Hence, in order to limit decarbonisation of pellets for electrochemical measurements, a further heat treatment at 1250 °C for 24 h with intermediate grinding followed by attrition milling and sieving (100µm) was adopted prior to pressing the powders in 10 mm-diameter cylindrical pellets and final firing at 1650 °C for 4-8 h.

Phase analysis was initially conducted by powder X-ray diffraction (XRD) on a Bruker D8 high-resolution diffractometer, using monochromatic Cu K α_1 radiation ($\lambda = 1.5406 \text{ \AA}$) obtained with a germanium monochromator. Neutron powder diffraction (NPD) measurements were performed on the high-resolution D2B diffractometer at the Institut Laue Langevin (Grenoble, France) on heating within a temperature range of 26 – 900 °C. A monochromatic beam wavelength of 1.594 Å was selected from the primary beam with a Ge monochromator. Synchrotron radiation X-ray diffraction (SR-XRD) was performed in the temperature range RT – 900 °C on the D10B-XRD1 beamline at the National Synchrotron Light Laboratory (LNLS, Campinas, Brazil). Data were collected in the range $20 \leq 2\theta \leq 90^\circ$ employing a wavelength of 1.54915 Å, a step length of 0.005 and a step counting time of 2 s. Samples were heated at a rate of 10 K.min⁻¹, and a dwell time of 10 min was adopted at each temperature before collecting the scan. Structural refinements of the NPD and SR-XRD data were performed by the Rietveld method with the Fullprof program²⁷.

A magnetic measurement system (MPMS-XL) was used in order to obtain the temperature dependence of the molar magnetic susceptibility χ of Ba(Ce_{0.2}Zr_{0.7})_(1-x/0.9)Pr_xY_{0.1}O_{3- δ} for the compositions $x = 0.225, 0.445$ and 0.9 . Polycrystalline samples were cooled down in zero field from room temperature to 2 K and then dc magnetization (M) was measured during warming the samples up to 300 K with an applied magnetic field (H) of 100 mT. χ was calculated as M/H taking into account the measured mass (~ 200 mg), the molecular weight (~ 300 g mol⁻¹) and the diamagnetic contribution ($\sim -75 \times 10^{-6}$ emu mol⁻¹ Oe⁻¹) of each sample.

Thermogravimetric analysis (TGA) was performed in synthetic air on heating at $20\text{ }^{\circ}\text{C}\cdot\text{min}^{-1}$ in the temperature range RT- $1030\text{ }^{\circ}\text{C}$ then cooling. A further heating cycle was then undertaken in 100% CO_2 to check stability versus the formation of BaCO_3 . The products of the TGA cycles were examined by XRD.

The faces of pellets for electrical measurements were coated with Heraeus Pt paste (CL11-5349) fired at $900\text{ }^{\circ}\text{C}$ for 1 hour to remove the organic content, harden the Pt and form attached unipotential electrode surfaces. Impedance spectroscopy was performed employing a signal amplitude of 50 mV in potentiostatic mode with an Autolab PGStat302N instrument operating over the frequency range $0.1 \leq f \leq 10^6\text{ Hz}$. The temperature dependence of conductivity was determined from data collected on cooling in steps of $50\text{ }^{\circ}\text{C}$ in the temperature range $150 - 900\text{ }^{\circ}\text{C}$ in wet and dry atmospheres of air and N_2 . Dry gas was fed from the bottle through a drying column containing a commercial moisture trap of aluminosilicate- and zeolite-based beads. For wet atmospheres, the gas was firstly bubbled through H_2O at room temperature to provide a water content of $\sim 0.023\text{ atm}$. Analysis of impedance spectra was performed with the Zview 2.9c software (Scribner Associates) by fitting the data to appropriate equivalent circuits in order to resolve the impedance response into bulk, grain-boundary and electrode contributions.

Results and Discussion

Phase Formation and RT structures

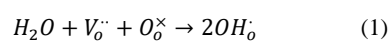
The XRD peaks of the series sintered at $1350\text{ }^{\circ}\text{C}$ revealed solid-solution formation for the whole series with somewhat broad peaks suggesting cubic or pseudo-cubic perovskite phases. On sintering at $1500\text{ }^{\circ}\text{C}$, sharper peaks indicated both enhanced crystallinity and more complex structural detail, with peak splitting particularly apparent for the Pr-rich end of the series.

Tilting of the octahedra in the perovskite structure gives rise to superlattice reflections associated with concerted oxygen movements, which are typically imperceptible to XRD due to the

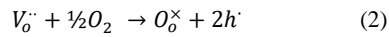
low X-ray oxygen scattering factor. Similarly, any slight distortion of the cation substructure may give rise to peak splitting which is difficult to observe by laboratory-diffraction techniques. High-resolution neutron powder diffraction is, thus, one of the most useful tools for precise determination of the space group in perovskites which display subtle phase transitions. This has been demonstrated for the end-member phases of the present series^{19,26}, which reach cubic symmetry on heating through three or four transitions in the sequence $Pnma \rightarrow Imma \rightarrow R\bar{3}c \rightarrow Pm\bar{3}m$ for BZCY72 ($Imma$ at RT) and $BaPr_{0.9}Y_{0.1}O_{3-\delta}$ ($Pnma$ at RT), respectively .

The NPD patterns of the series revealed distortions from the cubic perovskite aristotype as indicated by the presence of superlattice reflections, shown in Fig. 1 for $x = 0.225$ and $x = 0.445$. Indexing of these peaks in accordance with the method of Glazer²⁸ and Woodward and Reaney²⁹ followed a $\frac{1}{2}\{o\ o\ o\}$ pattern on the basis of the simple cubic unit cell, where ‘o’ represents an odd-number index. This type of reflection is compatible with antiphase tilting only of the octahedra, limiting the possible space groups to $I4/mcm$, $Imma$ and $R\bar{3}c$ ³⁰. The final choice of symmetry was made on analysis of the superstructure reflections originating from the distortion of the cubic perovskite phase, and inspection of the corresponding quality criteria of the refinement.

Fitting of the NPD data was performed using the appropriate orthorhombic, rhombohedral or cubic structural model, employing the nominal cation stoichiometries. No superlattice reflections related to a possible cation ordering on the perovskite B site were identified. Refinements were thus carried out assuming a statistical distribution of the B-site cations. Assuming the IV valence state for all B-site cations except Y3+ the nominal oxygen stoichiometry is expected to be 2.95. Refinement of the oxygen occupancies was performed leading to values which were generally higher than this nominal value, particularly in the low-temperature range (< 300 °C). This less-than-nominal oxygen deficiency may be due to partial hydration under normal synthesis conditions:



as occurs for the Pr-free BZCY72 end-member phase²⁶. However, oxygen occupancies may increase as well due to oxidation according to the following defect reaction:



High oxygen occupancies at lower temperatures indicate that the Pr and Ce cations are likely to be in the IV oxidation state; this is discussed in more detail in the following section. The fittings were also noticeably improved on employment of anisotropic temperature factors. The final structural parameters of the RT phases of $x = 0.225, 0.445$ and 0.9 are presented in Table 1. The observed and calculated NPD patterns of the series at RT and their differences are shown in Fig. 2.

Magnetic measurements and Pr oxidation state

Increasing magnetic susceptibility with decreasing temperature is observed for three selected samples in the $Ba(Ce_{0.2}Zr_{0.7})_{1-x}Pr_xY_{0.1}O_{3-\delta}$ series, Fig. 3, revealing that they are paramagnetic below RT. The paramagnetism ranges down to 2 K for compositions $x = 0.225$ and $x = 0.445$ but only to 9.5 K for $x = 0.9$ because of a sharp increase of χ at this temperature denoting the onset of magnetic interactions. Such interactions are most probably similar to those found in $BaPrO_3$, which develops antiferromagnetic ordering with a weak ferromagnetic component at 11.7 K¹. The partial substitution of paramagnetic Pr^{4+} cations by diamagnetic Y^{3+} in BPO ($x = 0.9$) and diamagnetic species Zr^{4+}/Ce^{4+} and Y^{3+} in the other series members is likely to account for the fall in the ordering temperature down to 9.5 K and 2 K, respectively.

On the other hand, the χ^{-1} vs T plot for the three samples (inset of Fig. 3) is not a straight line, indicating that χ follows a Curie-Weiss law in the paramagnetic region:

$$\chi = \frac{C}{T-\theta} \quad (3)$$

where C is the Curie constant corresponding to the Pr^{4+} ion and θ is the Weiss temperature expressing the exchange interactions between such ions. The best fit of the χ vs T curves above 60 K to the function

$$\chi(T) = \frac{C}{T-\theta} + \chi_0 \quad (4)$$

yields the fitting parameters listed in Table 2, which includes the magnetic moment per mole of Pr, μ , calculated from the experimental Curie constant; χ_0 is the so-called Van Vleck paramagnetism or temperature-independent paramagnetism (TIP) associated with Pr^{4+} . The high value of χ_0 obtained for the three samples is typical of a Pr^{4+} ion in an octahedral site where the crystal field and spin-orbit interaction effects are comparable². This situation can further reduce the magnetic moment of Pr^{4+} to a value much smaller than $2.54 \mu_B$, expected for a free Pr^{4+} ion in its $J=5/2$ ground state³. The small values of the experimental μ (Table 2) are consistent with the values of $\sim 0.70 \mu_B$ ^{2,4} and $\sim 0.85 \mu_B$ ^{5,6} previously obtained from magnetic-susceptibility measurements for BaPrO_3 . The analysis of the magnetic data obtained for the three samples denotes, therefore, the presence of praseodymium exclusively in a tetravalent state as paramagnetic cation located in an octahedral site. We note that Pr^{4+} on the perovskite A site is expected to have a magnetic moment closer to $2.54 \mu_B$ ⁶.

A lower quantity of Pr^{3+} species with increasing Pr content may be understood based on tolerance factor:

$$t = \frac{r_{A^{3+}} + r_O}{\sqrt{2}(r_{B^{3+}} + r_O)} \quad (5)$$

where r_A , r_B and r_O refer to the ionic radii of A, B and oxide ions respectively³¹. A lower tolerance factor is generally associated with poorer phase stability³². An increasing Pr content on the B site in either III or IV oxidation state, with larger ionic radii than the substituted Ce/Zr ratio, lowers the tolerance factor with increasing x . In the same way, placing Pr with lower ionic radius than Ba on the A site decreases t . Hence, with increasing x , Pr in the III oxidation state on either A or B sites would lower both t and phase stability even further.

Similarly low quantifications for Pr^{3+} species were previously found for the $\text{BaZr}_{1-x}\text{Pr}_x\text{O}_{3-\delta}$ system, with the slow kinetics of Pr^{3+} distribution on the A sites rationalized in terms of the combined requirements of cation-site redistribution, annihilation of unit cells, and volatilization of BaO^{22} . Note that this study reports a reduced lattice parameter in the case of a sample sintered at high temperature in reducing conditions, with a Pr^{3+} content of 11%. However, for this system and the present, the magnetic moments and lattice parameters concord that Pr is overwhelmingly present in the Pr IV oxidation state on sintering in air.

Phase Transitions and Phase Fields

The phase transitions exhibited with composition at RT result from increasing tilting of the layers of the BO_6 octahedra with increasing Pr content. This may be understood on the basis that the A ions are progressively undersized and the Goldschmidt tolerance factor becomes increasingly lower (eq.(5)). The effect of temperature is to partially release the stress associated with the mismatch of the A-O and B-O bond lengths through differentiated expansion of the A-O and B-O bonds leading to higher symmetry structures. The phase transitions, which occur on heating selected compositions in the title series in the temperature range RT – 900 °C, were studied by NPD using the same diagnostic procedure for indexation and determination of space group as employed earlier. As expected **from** consideration of **the** tolerance factor, high-symmetry phases are stabilized at high temperature and for lower Pr content.

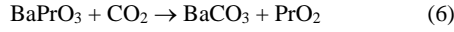
The transformation to cubic symmetry which occurs for all series members may be followed with increasing temperature on calculation of the octahedral tilt angle (ϕ) from the refined oxygen position of the hexagonal cell.³³ The temperature dependence of ϕ provides information on the continuous transition from $R\bar{3}c$ to $Pm\bar{3}m$, which may be second-order or tricritical in nature according to whether ϕ follows a $(T_c - T)^\beta$ temperature dependency with exponent of 0.5 or 0.25, respectively³⁴. The linear relationship near the transition temperature observed between ϕ^2 and T in the case of $x = 0.445$ (Fig. 4) indicates that the dependency of the tilt angle with temperature is better fit with an exponent of $\beta = 0.5$ in accordance with a second-order phase transition in this case.

Thermal evolution in air and CO₂

The pseudo-cubic lattice parameters of the series, determined from either NPD data collected in low vacuum or SR-XRD data in synthetic air, are shown in Fig. 5. As observed in our previous work of the BZCY72 end-member³⁵, the Vegard's plots exhibit non-linear behaviour, particularly apparent for the Ce/Zr-rich members, which may be attributable to more than one factor. The contraction exhibited for the end-member BZCY72 phase has been ascribed to a dehydration, which occurs for other proton-conducting perovskites^{36,37}; a similar dehydration may occur for the $x = 0.225$ phase up to 300 °C. (The last long sentence is not clear to me: In figure 5 one sees that the $x=0$ and $x=0.225$ compounds expand on heating up to about 300°C. You use the word "contraction" therefore you look in direction of cooling. This means that you say that on cooling these systems see a contraction because of dehydration: This is not clear to me. You can have dehydration on heating in a dry atmosphere and therefore a contraction or a hydration in a humid atmosphere and therefore expansion). We note that recent computer simulations indicate that chemical expansion results only from radius expansion of the reduced cation, whereas the formation of an oxygen vacancy leads to an opposing effect³⁸. When the loss of water results from dehydration (eq.(1)) with no reduction occurring we may, thus, expect the volume contraction shown in Fig. 5 for $x = 0$ and $x = 0.225$. Later members of the series do not

exhibit a pronounced non-linearity although deviations may arise on undergoing a first-order phase transformation from orthorhombic to rhombohedral symmetry. Thermal expansion coefficients (TECs) are listed in Table 3 for a low-temperature (LT) range, in which the samples may, to varying degrees, retain a non-trivial amount of water from hydration (eq. (1)), and a high temperature (HT) state, in the range 600-900 °C, after the dehydration event. The expansion on heating, most notable for the early series members, is greater in the hydrated state, which is also the case for proton-conducting $\text{BaCe}_{0.8}\text{Y}_{0.2}\text{O}_{2.9}$; interestingly, however, BaZrO_3 -based phases exhibit the opposite effect³⁷. In the high-temperature regime, there is a clear effect of Pr addition increasing TEC. This may be partly due to some reduction of Pr accompanied by oxygen loss at high temperature, which increases with x, as the neutron diffraction data and electrical conductivity (discussed later) indicate. However, the effect on lattice parameters appears to be very slight, suggesting such reduction is minimal. The much less apparent contraction on heating (Fig. 5) and converging of HT and LT TEC values (Table 3) of later series members may be understood to result from the lesser tendency towards hydration of BaPrO_3 -based perovskites. This may seem surprising, considering that, in BaBO_3 perovskites, there is generally a greater tendency towards hydration with increasing ionic radius (basicity) of the B cation³⁹. However, several studies have shown that hydration and proton transport in BaPrO_3 -based phases is inherently poor^{23,24,40}.

Mass loss as determined by thermogravimetry of the as-prepared samples on heating and cooling in synthetic air in the range RT – 900 °C varied within a narrow range, and did not provide a reliable determination of water content, partly due to the effect of absorbed species. Nevertheless, in accordance with the thermo-diffraction data, significant mass loss due to reduction of Pr^{4+} or Ce^{4+} species at higher temperature was not observed. In contrast, the TGA curves measured in CO_2 (Fig. 6) exhibited significant weight gain at ~ 530 °C for samples $x = 0.675$ and $x = 0.9$. X-ray diffraction of post-analysis samples indicated that reaction to form barium carbonate had taken place according to:



This result is similar to that of the $\text{Ba}(\text{Zr},\text{Pr},\text{Gd})\text{O}_{3-\delta}$ system^{24,41}, which is also increasingly less stable with greater Pr content. The poorer stability may be understood with reference to the present case on the basis that substitution of Ce/Zr for the Pr cation increases the average B cation radius, forming a more ionic B-O bond in which oxygen is more likely to act as an electron donor and react with acidic gases. Moreover, as discussed earlier, the effect of the substitution is to lower the tolerance factor, which is associated with structures of lower stability³². It may be suggested that the higher tolerance towards carbonation at high temperature results from increasing experimental tolerance factor as the mismatch between A-O and B-O bonds is reduced.

Electrical conductivity

Arrhenius plots for the total conductivity of the $\text{Ba}(\text{Ce}_{0.2}\text{Zr}_{0.7})(1-x/0.9)\text{Pr}_x\text{Y}_{0.1}\text{O}_{3-\delta}$ series in dry N_2 and air are shown in Fig. 7, with corresponding activation energies listed in Table 4. In both atmospheres, substitution of Pr for Zr/Ce in the range $0 \leq x \leq 1$ raises conductivity by over two orders of magnitude. A similar increase has been observed in the $\text{BaZr}_{1-x}\text{Pr}_x\text{O}_{3-\delta}$ solid solution⁴², as well as **in** related acceptor-doped systems such as $\text{BaZr}_{0.9-x}\text{Pr}_x\text{Gd}_{0.1}\text{O}_{3-\delta}$ ²⁴. Electrical transport in the acceptor-doped BaPrO_3 -based phase is attributed to electron holes^{19,43}. The substantial increase in conductivity with Pr content may be understood, therefore, to arise from increasing electronic conductivity. For all members of the series, conductivity is significantly higher in dry air in comparison to N_2 (Fig. 7(c) and (d)) in accordance with an ‘extrinsic’ model, in which the acceptor-dopant concentration is largely balanced by oxygen-vacancy formation, according to the electroneutrality condition

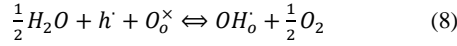
$$[Y'_{\text{Zr}}] = 2[v_o^{\bullet\bullet}] \quad (7)$$

Oxygen may then fill the vacancies in an oxidizing atmosphere giving rise to electron-hole transport according to eq. (2). When oxidation is the predominant defect equilibrium and the electroneutrality condition is that expressed in eq. (7) then the electronic conductivity follows a power-law dependency, $\sigma_e \propto \log pO_2^{+1/4}$.⁴⁴

The conductivity generally curves downward with increasing temperature for compositions of high Pr content. This “bending” has been explained as resulting from oxygen loss at high temperature, which is compensated by the consumption of holes (eq. (2) is driven to the left)⁴³. Accordingly, the oxygen occupancies refined from NPD data were found to decrease at higher temperature (data not shown). This behaviour is thus fully consistent with predominant electron-hole conductivity.

The hole species may be considered as residing in the oxygen band rather than resulting from mixed-valence cation states, as indicated by the magnetic measurements and neutron refinements of the oxygen occupancies. The high hole concentration precludes the ready assignment of a purely small-polaron, thermally-activated model at high temperature, where some itinerant character may prevail. At lower temperature (250- 500 °C), however, the activation energy, ~0.5-0.7 eV (Table 4), suggests that small polarons are dominant in this regime. Stokes and Islam⁴⁵ have modelled O^\cdot in $BaPrO_3$ as the conducting species in oxidizing conditions. We note that several, if not all, acceptor-doped proton-conducting perovskites, such as $BaCeO_3$ - and $SrZrO_3$ -based phases also exhibit significant p-type conductivity in dry oxidizing conditions^{46,47}. An interesting occurrence is that substitution of Ce/Zr with Pr^{4+} , with an ionic radius intermediate between that of Ce^{4+} and Zr^{4+} promotes much greater electronic conductivity at the expense of proton conductivity⁴⁸.

Comparison of conductivities in wet and dry conditions, Fig. 8, reveals slightly lower transport in wet air than dry for the Pr-doped samples (Fig. 8(b)), although the difference between wet and dry conditions is minimal for $x = 0.225$ (Fig. 8(a)). Such behaviour is again consistent with predominant electron-hole transport due to the consumption of holes with less-mobile protons under wet atmospheres according to



However, the BZCY sample exhibits greater conductivity in humidified in comparison to dry air, particularly at lower temperature, indicative of a considerable protonic contribution to transport (Fig.8(a)), as has been recently confirmed by an analysis of the transport carriers on varying oxygen and water-vapour partial pressures⁴⁹. Similar results are observed in dry and wet N₂ for the Pr-doped samples as in air (Fig. 8 (d)), with the exception of the x = 0.225 sample (Fig. 8(c)). In this case, the much lower hole conductivity in the “extrinsic” regime means that protons are likely to participate in transport in wet conditions, as is the case for the BZCY72 phase. The observance of a dehydration event influencing the lattice parameter of this sample (Fig. 5) supports the premise that protons are influential species on electrical transport in compositions of low Pr content.

Conclusions

Substitution of Ce/Zr cations with Pr in the technologically relevant BaZr_{0.7}Ce_{0.2}Y_{0.1}O_{3-δ} perovskite leads to enhanced electronic conductivity, desired for membrane and fuel-cell cathode applications. The BaZr_{0.7}Ce_{0.2}Y_{0.1}O_{3-δ}-BaPr_{0.9}Y_{0.1}O_{3-δ} system forms a complete solid solution, exhibiting symmetry changes in the sequence $Pnma \rightarrow Imma \rightarrow R\bar{3}c \rightarrow Pm\bar{3}m$. Higher symmetry is favoured for lower Pr content and higher temperature, as expected from tolerance-factor considerations. The exclusive presence of Pr on the B site in the IV oxidation state is confirmed by magnetic measurements. Increasing electrical transport with increasing Pr content is thus ascribed to small polaronic hopping in the oxygen band rather than mixed Pr valence states. Charge compensation follows an ‘extrinsic’ model in which oxygen vacancies compensate the acceptor dopant. Refinement of neutron-diffraction data supports a model for the latter compositions of filled nominal oxygen sites, with concomitant formation of holes. Conversely, low Pr content is associated with transport behaviour

more similar to that of the BZCY72 end-member phase, with higher conductivity exhibited in humidified in comparison to dry N₂ and contraction of unit-cell parameter on heating attributable to dehydration.

Acknowledgements

This work was supported by the MINECO, Spain (ENE2015-66183-R), CSIC, Spain (i-link0743), and CAPES, Brazil (PVE, Proceso 88881.03418/2013-1). Access to the neutron facilities at the Institut Laue Langevin (Grenoble, France) and the National Synchrotron Light Laboratory (LNLS, Campinas, Brazil) under grant 5-24-55(D2B) and research proposal D10B-XRD1-16166, respectively, is gratefully acknowledged. U.A. also thanks MINECO (MAT2016-78362-C4-1-R) and the Universidad San Pablo for financial support.

Figure Captions

1. Experimental (circles) and calculated (continuous line) neutron diffraction patterns of the $\text{Ba}(\text{Zr}_{0.7}\text{Ce}_{0.2})_{(1-x/0.9)}\text{Pr}_x\text{Y}_{0.1}\text{O}_{3-\delta}$ series for (a) $x = 0.225$ and (b) $x = 0.445$ collected at RT with an incident wavelength of 1.594 \AA . The panels indicate superstructure reflections with a $\frac{1}{2}\{o\ o\}$ indexation (where “o” indicates an index with an odd number) resulting from antiphase tilting.
2. Experimental (circles), calculated (continuous line) and difference (continuous line at bottom of each panel) neutron diffraction patterns for (a) $x = 0.225$ and (b) $x = 0.445$ of the $\text{Ba}(\text{Zr}_{0.7}\text{Ce}_{0.2})_{(1-x/0.9)}\text{Pr}_x\text{Y}_{0.1}\text{O}_{3-\delta}$ series collected at RT with an incident wavelength of 1.594 \AA ; the positions of Bragg peaks are indicated by vertical bars.
3. Temperature dependence of the magnetic susceptibility per formula unit in an applied magnetic field of 100 mT for $\text{Ba}(\text{Zr}_{0.7}\text{Ce}_{0.2})_{(1-x/0.9)}\text{Pr}_x\text{Y}_{0.1}\text{O}_{3-\delta}$ oxides with $x = 0.9$ (hexagons), $x = 0.445$ (diamonds) and $x = 0.225$ (circles). The inset shows the corresponding χ^{-1} vs T plots.
4. The square of the octahedral tilt angle (ϕ) of $x = 0.445$ as a function of temperature, (squares, primary y-axis), and ϕ as a function of temperature (circles, secondary y-axis) fitted with the power law $\phi = (1 - \frac{T}{T_c})^{0.5}$ suggesting a second-order phase transitions.
5. Pseudo-cubic lattice constants of the $\text{Ba}(\text{Zr}_{0.7}\text{Ce}_{0.2})_{(1-x/0.9)}\text{Pr}_x\text{Y}_{0.1}\text{O}_{3-\delta}$ series determined from neutron diffraction data on heating in low vacuum and determined from synchrotron X-ray diffraction data on heating in synthetic air.
6. TGA plots for the $\text{Ba}(\text{Zr}_{0.7}\text{Ce}_{0.2})_{(1-x/0.9)}\text{Pr}_x\text{Y}_{0.1}\text{O}_{3-\delta}$ series in 100% CO_2 with a heating rate of $20 \text{ }^\circ\text{C}\cdot\text{min}^{-1}$.
7. Temperature dependence of total conductivity for the $\text{Ba}(\text{Zr}_{0.7}\text{Ce}_{0.2})_{(1-x/0.9)}\text{Pr}_x\text{Y}_{0.1}\text{O}_{3-\delta}$ series in dry air and N_2 .
8. Temperature dependence of total conductivity for the $\text{Ba}(\text{Zr}_{0.7}\text{Ce}_{0.2})_{(1-x/0.9)}\text{Pr}_x\text{Y}_{0.1}\text{O}_{3-\delta}$ series in atmospheres of (a) dry and humidified air for $x = 0$ and $x = 0.225$ (b) dry and humidified air for $x \geq 0.445$ (c) dry and humidified N_2 for $x = 0$ and $x = 0.225$ and (d) dry and humidified air for $x \geq 0.445$

Table 1. Structural parameters, interatomic distances up to 3.5 Å and agreement factors for Ba(Zr_{0.7}Ce_{0.2})_(1-x/0.9)Pr_xY_{0.1}O_{3.δ} obtained from NPD data.

	0.225 (R$\bar{3}c$)^{a,d}	0.445 (Imma)^{b,e}	0.9 (Pnma)^{c,f}
<i>a</i> (Å)	6.0574(3)	6.0828(4)	6.1737(2)
<i>b</i> (Å)	6.0574(3)	8.6217(7)	8.7164(2)
<i>c</i> (Å)	14.807(1)	6.1107(4)	6.2075(1)
<i>V</i> (Å³)	470.50(5)	320.47(4)	334.04(1)
<i>Ba</i> position	6a	4e	4c
<i>X</i>	-	-	0.010(1)
<i>Y</i>	-	-	-
<i>Z</i>	-	-0.0068(4)	0.0036(6)
<i>U</i>_{iso} × 100 (Å²)	1.1(1)	0.74(3)	1.04(4)
<i>Zr/Pr/Y</i> position	6b	4b	4b
<i>U</i>_{iso} × 100 (Å²)	0.43(2)	0.57(3)	0.61(4)
<i>O</i>(1) position	18c	4e	4c
<i>x</i>	0.4648(2)	-	0.494(1)
<i>z</i>	-	-0.0577(4)	-0.0680(4)
<i>Occ</i>	2.95(1)	1.00	0.97(1)
<i>U</i>_{iso} × 100 (Å²)	1.79(4)	1.61(4)	1.5(1)
<i>O</i>(2) position	-	8g	8d
<i>x</i>	-	-	0.2669(5)
<i>y</i>	-	-0.0210(5)	0.4641(2)
<i>z</i>	-	-	0.2676(5)
<i>Occ</i>	-	1.99(1)	2.00(1)
<i>U</i>_{iso} × 100 (Å²)	-	2.00(6)	2.0(1)
Selected distances (Å)			
<i>Ba-O</i>(1)	3.241(1) × 3	3.057(1) × 2	3.215(9) × 1
	2.816 (1) × 3	2.661(1) × 1	3.022(9) × 1
	3.0320(7) × 6	3.449(1) × 1	2.706(4) × 1
<i>Ba-O</i>(2)		3.160(1) × 4	2.948(5) × 2
		2.945(1) × 4	2.783(5) × 2
			3.203(4) × 2
Average <i>Ba-O</i>	3.0303(8)	3.018(1)	2.979(2)
<i>Zr/Pr/Y-O</i>(1)	2.1507(9) × 6	2.184(1) × 2	2.2199(5) × 2
<i>Zr/Pr/Y-O</i>(2)		2.163(1) × 4	2.220(3) × 2
			2.212(3) × 2
Average <i>Zr/Pr/Y-O</i>	2.1507(9)	2.170(1)	2.217(1)
<i>t</i>-factor	0.9965	0.9834	0.9501

^a Space Group $R\bar{3}c$, (# 167): 6a (0 0 $\frac{1}{4}$), 6b (0 0 0), 18e (x 0 $\frac{1}{4}$)

^b Space Group $Imma$, (# 74): 4b (0 $\frac{1}{2}$ $\frac{1}{2}$), 4e (0 $\frac{1}{4}$ z), 8g ($\frac{1}{4}$ y $\frac{3}{4}$)

^c Space Group $Pnma$, (# 62): 4c (x $\frac{1}{4}$ z), 4b (0 0 $\frac{1}{2}$), 8d (x y z)

^d $\chi^2=1.31$, $R_{exp}=3.24\%$, $R_{wp}=3.71\%$, $R_B=1.58\%$,

Composition: Ba(Zr_{0.525}Ce_{0.15})Pr_{0.225}Y_{0.1}O_{2.95(1)}, $\rho_{(cryst)}: 6.23(5)$ g/cm³

^e $\chi^2=1.85$, $R_{exp}=3.07\%$, $R_{wp}=4.20\%$, $R_B=2.02\%$,

Composition: Ba(Zr_{0.354}Ce_{0.101})Pr_{0.445}Y_{0.1}O_{3.00(1)}, $\rho_{(cryst)}: 6.29(5)$ g/cm³

^f $\chi^2=1.47$, $R_{exp}=2.93\%$, $R_{wp}=3.56\%$, $R_B=3.10\%$,

Composition: BaPr_{0.900}Y_{0.100}O_{2.97(1)}, $\rho_{(cryst)}: 6.37(5)$ g/cm³

Table 2. Magnetic data for the $\text{Ba}(\text{Zr}_{0.7}\text{Ce}_{0.2})_{(0.9-x)/0.9}\text{Pr}_x\text{Y}_{0.1}\text{O}_{3-\delta}$ series: Curie constant C , Weiss constant θ and temperature-independent paramagnetism χ_0 obtained from the fit of the experimental magnetic susceptibility to eq.(4). Magnetic moment μ calculated as $\sqrt{8C}$.

x	C (emu K mol Pr ⁻¹ Oe ⁻¹) ^a	θ (K)	χ_0 (emu mol Pr ⁻¹ Oe ⁻¹) ^a	μ (μ_B)
0.900	$5.280(1)\times 10^{-2}$	-10.8(2)	$6.252(3)\times 10^{-4}$	0.68(2)
0.445	$7.139(9)\times 10^{-2}$	-6.1(2)	$6.202(3)\times 10^{-4}$	0.76(3)
0.225	$8.942(6)\times 10^{-2}$	-2.9(2)	$6.716(2)\times 10^{-4}$	0.85(3)

^a Values were obtained by dividing those obtained from the fitting for the x value in order to express the results per mole of praseodymium instead of per mole of compound.

Table 3. Thermal expansion coefficients for the $\text{Ba}(\text{Zr}_{0.7}\text{Ce}_{0.2})_{(1-x)/0.9}\text{Pr}_x\text{Y}_{0.1}\text{O}_{3-\delta}$ series in air

x	composition	TEC LT range (K ⁻¹ /10 ⁻⁶) ^a	TEC HT range (K ⁻¹ /10 ⁻⁶) ^b
0	$\text{Ba}(\text{Zr}_{0.7}\text{Ce}_{0.2}\text{Y}_{0.1})\text{O}_{3-\delta}$	12.72	7.18
0.225	$\text{Ba}(\text{Zr}_{0.525}\text{Ce}_{0.15}\text{Pr}_{0.225}\text{Y}_{0.1})\text{O}_{3-\delta}$	18.65	7.74
0.445	$\text{Ba}(\text{Zr}_{0.354}\text{Ce}_{0.101}\text{Pr}_{0.445}\text{Y}_{0.1})\text{O}_{3-\delta}$	14.91	9.43
0.675	$\text{Ba}(\text{Zr}_{0.175}\text{Ce}_{0.05}\text{Pr}_{0.675}\text{Y}_{0.1})\text{O}_{3-\delta}$	14.50	10.09

^a TECs determined from SR-XRD in the range RT-300 °C for $x = 0$ and RT-250°C for all other samples

^b TECs determined from SR-XRD in the range 600-900 °C for all samples

Table 4. Activation energy (in eV) of electrical conductivity for the $\text{Ba}(\text{Zr}_{0.7}\text{Ce}_{0.2})_{(1-x)/0.9}\text{Pr}_x\text{Y}_{0.1}\text{O}_{3-\delta}$ series in as a function of Zr concentration, in dry and humidified air and N₂ atmospheres in the temperature range 250 – 500 °C.

x	dry		wet	
	air	N ₂	air	N ₂
0	1.0	0.84	0.74	0.69

0.225	0.56	0.52	0.58	0.51
0.445	0.51	0.44	0.55	0.44
0.675	0.41	0.40	0.46	0.40
0.9	0.43	0.33	0.48	0.40

References

- 1 H. Iwahara, *Solid State Ionics*, 2004, **168**, 299–310.
- 2 T. Norby and Y. Larring, *Solid State Ionics*, 2000, **137**, 139–148.
- 3 E. Fabbri, L. Bi, D. Pergolesi and E. Traversa, *Adv. Mater.*, 2012, **24**, 195–208.
- 4 K. Xie, Y. Zhang, G. Meng and J. T. S. Irvine, *J. Mater. Chem.*, 2011, **21**, 195.
- 5 H. Matsumoto, S. Okada, S. Hashimoto, K. Sasaki, R. Yamamoto, M. Enoki and T. Ishihara, *Ionics (Kiel)*, 2007, **13**, 93–99.
- 6 S. H. Morejudo, R. Zanon, S. Escolastico, I. Yuste-Tirados, H. Malerod-Fjeld, P. K. Vestre, W. G. Coors, A. Martinez, T. Norby, J. M. Serra and C. Kjolseth, *Science*, 2016, **353**, 563–566.
- 7 W. G. Coors, *J. Power Sources*, 2003, **118**, 150–156.
- 8 L. Bi, S. Boulfrad and E. Traversa, *Chem. Soc. Rev.*, 2014, **43**, 8255–8270.
- 9 S. Robinson, a. Manerbino, W. Grover Coors and N. P. Sullivan, *Fuel Cells*, 2013, **13**, 584–591.
- 10 E. Vasileiou, V. Kyriakou, I. Garagounis, a. Vourros and M. Stoukides, *Solid State Ionics*, 2015, **275**, 110–116.
- 11 J. Dailly, S. Fourcade, a. Largeteau, F. Mauvy, J. C. Grenier and M. Marrony, *Electrochim. Acta*, 2010, **55**, 5847–5853.
- 12 S. Ricote, N. Bonanos, F. Lenrick and R. Wallenberg, *J. Power Sources*, 2012, **218**, 313–319.
- 13 W. Sun, L. Yan, B. Lin, S. Zhang and W. Liu, *J. Power Sources*, 2010, **195**, 3155–3158.
- 14 L. Bi, E. Fabbri and E. Traversa, *Solid State Ionics*, 2012, **214**, 1–5.
- 15 E. Fabbri, I. Markus, L. Bi, D. Pergolesi and E. Traversa, *Solid State Ionics*, 2011, **202**, 30–35.
- 16 R. Strandbakke, V. A. Cherepanov, A. Y. Zuev, D. S. Tsvetkov, C. Argirusis, G. Sourkouni, S. Pr??nte and T. Norby, *Solid State Ionics*, 2015, **278**, 120–132.

- 17 L. Yang, Z. Liu, S. Wang, Y. Choi, C. Zuo and M. Liu, *J. Power Sources*, 2010, **195**, 471–474.
- 18 E. Fabbri, L. Bi, D. Pergolesi and E. Traversa, *Energy Environ. Sci.*, 2011, **4**, 4984.
- 19 C. S. Knee, A. Magrasó, T. Norby and R. I. Smith, *J. Mater. Chem.*, 2009, **19**, 3238.
- 20 Z. Wang, M. Liu, W. Sun, D. Ding, Z. Lü and M. Liu, *Electrochem. commun.*, 2013, **27**, 19–21.
- 21 E. Fabbri, L. Bi, H. Tanaka, D. Pergolesi and E. Traversa, *Adv. Funct. Mater.*, 2011, **21**, 158–166.
- 22 I. Antunes, S. Mikhalev, G. C. Mather, V. V. Kharton, F. G. Figueiras, A. Alves, J. Rodrigues, M. R. Correia, J. R. Frade and D. P. Fagg, *Inorg. Chem.*, 2016, **55**, acs.inorgchem.6b01084.
- 23 A. Magrasó, F. Espiell, M. Segarra and J. T. S. Irvine, *J. Power Sources*, 2007, **169**, 53–58.
- 24 A. Magrasó, C. Frontera, A. E. Gunnæs, A. Tarancón, D. Marrero-López, T. Norby and R. Haugsrud, *J. Power Sources*, 2011, **196**, 9141–9147.
- 25 I. Antunes, G. C. Mather, J. R. Frade, J. Gracio and D. P. Fagg, *J. Solid State Chem.*, 2010, **183**, 2826–2834.
- 26 G. C. Mather, G. Heras-Juaristi, C. Ritter, R. O. Fuentes, A. L. Chinelatto, D. Pérez-Coll and U. Amador, *J. Mater. Chem. A*, 2016.
- 27 J. Rodriguez-Carvajal, *Phys. B*, 1993, **192**, 55–69.
- 28 A. M. Glazer, *Acta Crystallogr. Sect. A*, 1975, **31**, 756–762.
- 29 D. I. Woodward and I. M. Reaney, *Acta Crystallogr. B.*, 2005, **61**, 387–99.
- 30 C. J. Howard and H. T. Stokes, *Acta Crystallogr. Sect. B Struct. Sci.*, 1998, **54**, 782–789.
- 31 R. D. Shannon, *Acta Crystallogr. Sect. A*, 1976, **32**, 751–767.
- 32 H. Yokokawa, T. Kawada and M. Dokiya, *J. Am. Ceram. Soc.*, 1989, **72**, 152–153.
- 33 C. J. Howard, B. J. Kennedy and B. C. Chakoumakos, *J. Phys. Condens. Matter*, 2000, **12**, 349–365.

- 34 M. Glerup, K. S. Knight and F. W. Poulsen, *Mater. Res. Bull.*, 2005, **40**, 507–520.
- 35 G. C. Mather, G. Heras-Juaristi, C. Ritter, R. O. Fuentes, A. L. Chinelatto, D. Pérez-Coll and U. Amador, *Chem. Mater.*, 2016, **28**, 4292–4299.
- 36 C. Hiraiwa, D. Han, A. Kuramitsu, A. Kuwabara, H. Takeuchi, M. Majima and T. Uda, *J. Amercian Ceram. Soc.*, 2013, **884**, 879–884.
- 37 A. K. E. Andersson, S. M. Selbach, C. S. Knee and T. Grande, *J. Am. Ceram. Soc.*, 2014, **2661**, 2654–2661.
- 38 D. Marrocchelli, S. R. Bishop, H. L. Tuller and B. Yildiz, 2012, 1958–1965.
- 39 K. D. Kreuer, *Annu. Rev. Mater. Res.*, 2003, **33**, 333–359.
- 40 K. A. Furoy, R. Haugrud, M. Hänsel, A. Magrasó and T. Norby, *Solid State Ionics*, 2007, **178**, 461–467.
- 41 A. Magrasó, X. Solans, J. T. S. Irvine and M. Segarra, *Ceram. Int.*, 2009, **35**, 1819–1827.
- 42 I. Antunes, U. Amador, A. Alves, M. R. Correia, C. Ritter, J. R. Frade, D. Pérez-Coll, G. C. Mather and D. P. Fagg, *Inorg. Chem.*, 2017, **56**, 9120–9131.
- 43 A. Magrasó, R. Haugrud, M. Segarra and T. Norby, *J. Electroceramics*, 2008, **23**, 80–88.
- 44 N.-H. Chan, R. K. Sharma and D. M. Smyth, *J. Am. Ceram. Soc.*, 1982, **65**, 167–170.
- 45 S. J. Stokes and M. S. Islam, *J. Mater. Chem.*, 2010, **20**, 6258–6264.
- 46 S. Ricote, N. Bonanos, M. C. Marco de Lucas and G. Caboche, *J. Power Sources*, 2009, **193**, 189–193.
- 47 D. Pérez-Coll, G. Heras-Juaristi, D. P. Fagg and G. C. Mather, *J. Power Sources*, 2014, **245**, 445–455.
- 48 J. F. Basbus, M. Moreno, A. Caneiro and L. V. Mogni, *J. Electrochem. Soc.*, 2014, **161**, F969–F976.
- 49 G. Heras-Juaristi, D. Pérez-Coll and G. C. Mather, *J. Power Sources*, 2017, **364**, 52–60.

Magnetic references

- 1 N. Rosov, J. W. Lynn, Q. Lin, G. Cao, J. W. O'Reilly, P. Pernambuco-Wise and J. E. Crow, *Physical Review B*, 1992, **45**, 982-986.
- 2 M. Bickel, G. L. Goodman, L. Soderholm and B. Kanellakopoulos, *J. Solid State Chem.*, 1988, **76**, 178-185.
- 3 Y. Hinatsu and N. Edelstein, *J. Solid State Chem.*, 1994, **112**, 53-57.
- 4 Y. Hinatsu, *J. Solid State Chem.*, 1993, **102**, 362-367.
- 5 M. Itoh and Y. Hinatsu, *J. Alloys Compds.*, 1998, **264**, 119-124.
- 6 M. Itoh, K. Tezuka, M. Wakeshima and Y. Hinatsu, *J. Solid State Chem.*, 1999, **145**, 104-109.

Comentado [GM1]: I shall add these and any other additional references in the correct order before submission.